East Asian Journal on Applied Mathematics
doi: 10.4208/eajam.2022-257.041222

Vol. **xx**, No. x, pp. 1-25
xxx 2023

High-Order Spectral Difference Gas-Kinetic Schemes for Euler and Navier-Stokes Equations

Qing Xie[1], Xing Ji[2], Zihua Qiu[3], Chunlei Liang[4,5] and Kun Xu[1,6,7,*]

[1]*Department of Mathematics, Hong Kong University of Science and Technology, Clear Water Bay, Kowloon, Hong Kong SAR, China.*
[2]*Shaanxi Key Laboratory of Environment and Control for Flight Vehicle, Xi'an Jiaotong University, Xi'an, China.*
[3]*First Aircraft Institute of AVIC, Xi'an, China.*
[4]*Department of Mechanical and Aerospace Engineering, Clarkson University, New York, USA.*
[5]*The Center for Advanced Materials Processing, Clarkson University, New York, USA.*
[6]*Department of Mechanical and Aerospace Engineering, Hong Kong University of Science and Technology, Clear Water Bay, Kowloon, Hong Kong SAR, China.*
[7]*Shenzhen Research Institute, Hong Kong University of Science and Technology, Shenzhen, China.*

Received 17 September 2022; Accepted (in revised version) 4 December 2022.

Dedicated to Professor Tao Tang on occasion of his 60th birthday

Abstract. High-order spectral difference gas-kinetic schemes (SDGKS) are developed for inviscid and viscous flows on unstructured quadrilateral meshes. Rather than the traditional Riemann solver, the spectral difference method is coupled with the gas-kinetic solver, which provides a time-accurate flux function at the cell interface. With the time derivative of the flux function, a two-stage fourth-order time-stepping method is adopted to achieve high-order accuracy with fewer middle stages. The stability analysis for the linear advection equation shows that fourth-order spatial and temporal discretization SDGKS is stable under CFL condition. Quantitatively, the fourth-order SDGKS is around 8% more efficient than the traditional one with the Riemann solver and the strong stability preserving five-stage fourth-order Runge-Kutta method. Both steady and unsteady tests obtained by SDGKS compare well with analytic solutions and reference results.

AMS subject classifications: 52B10, 65D18, 68U05, 68U07

Key words: Spectral difference method, high-order method, gas-kinetic scheme, two-stage fourth-order time stepping, Navier-Stokes equation.

*Corresponding author. *Email addresses:* qxieab@connect.ust.hk (Q. Xie), jixing@xjtu.edu.cn (X. Ji), qzhnumber1@163.com (Z. Qiu), cliang@clarkson.edu (C. Liang), makxu@ust.hk (K. Xu)

 ©2023 Global-Science Press

1. Introduction

The high-order gas-kinetic schemes (GKS) under the finite volume framework have been developed in the last decade [10]. The GKS flux is based on a time evolution solution of the Bhatnagar-Gross-Krook (BGK) model [3]. Compared with traditional Riemann solver, the highlights of GKS include these:

i) The gas distribution function at interfaces contains the evolution from the upwind flux vector splitting to the central difference Lax-Wendroff type discretization.

ii) The inviscid and viscous fluxes are evaluated simultaneously.

iii) The GKS flux has multi-dimensional properties [34], where both normal and tangential derivatives of flow variables are involved in the time evolution of gas distribution function.

iv) The time-accurate gas evolution updates the solution at the cell interface which can be used in the construction of high-order compact schemes [38].

v) The multi-stage multi-derivative (MSMD) methods can be applied in GKS, and higher-order time accuracy with few middle stages can be achieved.

vi) The multi-scale unified GKS (UGKS) is also developed for the whole flow regime [13, 14].

The family of high-order GKS [8], based on the same WENO reconstruction, has favorable performance in efficiency, accuracy, and robustness, in comparison with the traditional high-order schemes with Riemann solver and Runge-Kutta (RK) time-stepping techniques. Owing to the multi-dimensional property in GKS flux, it captures flow structures, such as shear instabilities, much better than the schemes using the Riemann solver. Among those high-order GKS, the two-stage fourth-order method (S2O4) [21] seems to be the optimal choice and is efficient, accurate, and as robust as the second-order one. Besides, it has been applied to multicomponent flow [19], the direct simulation of compressible homogeneous turbulent flow [20], and hypersonic multi-temperature flow [4]. The high-order GKS has been successfully extended to the discontinuous Galerkin (DG) [16, 25, 26] and the correction procedure via reconstruction (CPR) [36] as well. And it has been applied within the finite difference framework on uniform grids [35]. In this paper, the high-order GKS will be developed on the unstructured quadrilateral meshes under the spectral difference framework for the first time.

The spectral difference (SD) method was firstly proposed in [15, 32] for simplex elements and has been studied in the past decades. It combines the advantages of finite-volume and finite-difference methods, such as geometric flexibility and high computational efficiency. The three-dimensional SD method has also been developed on hexahedral meshes by Sun *et al.* [29] and was used to simulate turbulent channel flow in [11, 23, 24]. However, the original form of the SD method is known to have instability on triangular elements, losing its popularity on simplex elements. Later, Balan *et al.* [1] proposed a stable

high-order spectral method by using Raviart-Thomas spaces (SDRT) for flux interpolation on triangular elements. The SDRT scheme has been studied in [5, 9, 12] for inviscid and viscous flows on triangular, quadrilateral, and mixed elements, and the accuracy and stability have been validated. Compared with DG and spectral volume (SV) methods, the formulation is simple since no test function or surface integral are involved.

Instead of the traditional Riemann solver and multi-stage RK method, the GKS solver with S2O4 time-stepping will be developed under the SD framework. Apart from the high-order values of the conservative variables at flux points, the derivatives are also needed in the gas-kinetic solver. They can be obtained by naturally extending the first approach of Bassi and Rebay (BR1) [2]. In this way, SDGKS can be easily implemented from the original SD method. With the help of the S2O4 method, 60% of iteration stages are saved in comparison with the strong-stability-preserving five-stage fourth-order Runge-Kutta method (sspRK5O4). The efficiency is high for the viscous flow computation by SDGKS under the same in-house FORTRAN code. The stability of SDGKS, together with the traditional one, will be carefully studied for the linear advection equation. And various numerical tests will be investigated to verify the accuracy and efficiency of the schemes.

The paper is organized as follows. Section 2 presents the SDGKS method and Section 3 shows the linear stability analysis for the numerical schemes. Section 4 is the numerical tests and Section 5 is the conclusion and the future work.

2. Spectral Difference Gas-Kinetic Schemes

2.1. SD spatial discretization

Consider the 2D conservation laws,

$$\frac{\partial \mathbf{W}}{\partial t}+\frac{\partial \mathbf{F}}{\partial x}+\frac{\partial \mathbf{G}}{\partial y}=0, \tag{2.1}$$

where $\mathbf{W}$ is the conservative variables, $\mathbf{F}$ and $\mathbf{G}$ are the fluxes. The physical domain is discretized with quadrilateral elements. And the quadrilateral elements are transformed into the standard square reference elements. The transformation between the physical element and the square element ($-1 \le \xi, \eta \le 1$) for the n-th element is

$$\mathbf{X}=\sum_{i=1}^{K} S_i(\xi,\eta)\mathbf{X}_{i,n},$$

where K is the number of points used to define the physical element, $\mathbf{X}_{i,n}$ are the Cartesian coordinates of those points, and $S_i(\xi,\eta)$ are shape functions. For elements with the $K=4$ straight edges in Fig. 1, the mapping function is

$$\begin{aligned}\mathbf{X}=&\frac{(1-\xi)(1-\eta)}{4}\mathbf{X}_{1,n}+\frac{(1+\xi)(1-\eta)}{4}\mathbf{X}_{2,n}\\&+\frac{(1+\xi)(1+\eta)}{4}\mathbf{X}_{3,n}+\frac{(1-\xi)(1+\eta)}{4}\mathbf{X}_{4,n}.\end{aligned}$$

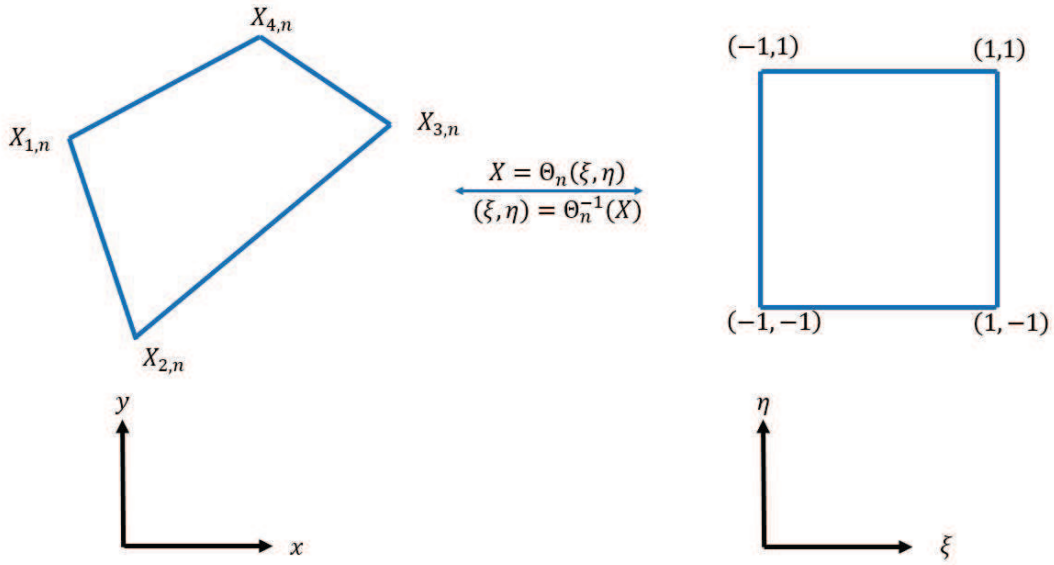

Figure 1: The Mapping from the physical domain (x, y) to the computational domain (ξ, η).

For elements on the curved boundaries, 8 points (four mid-edge and four corner points) can be used to define a quadratic representation and 12 points for a third-order cubic representation. The governing equation (2.1) is then transformed into the computational domain as

$$\frac{\partial \widetilde{\mathbf{W}}}{\partial t} + \frac{\partial \widetilde{\mathbf{F}}}{\partial \xi} + \frac{\partial \widetilde{\mathbf{G}}}{\partial \eta} = 0,$$

where $\widetilde{\mathbf{W}} = |J|\mathbf{W}$ and

$$\begin{pmatrix} \widetilde{\mathbf{F}} \\ \widetilde{\mathbf{G}} \end{pmatrix} = |J|J^{-1} \begin{pmatrix} \mathbf{F} \\ \mathbf{G} \end{pmatrix}.$$

The Jacobian matrix for the transformation is defined as

$$J = \begin{pmatrix} x_\xi & x_\eta \\ y_\xi & y_\eta \end{pmatrix}.$$

The metrics and the Jacobian matrix are computed for each element.

Two kinds of points are placed on the element: solution points and flux points. Gauss-Legendre-quadrature-point locations and two end points $-1, 1$ are used for the flux points in order to avoid the weak instability caused by using Chebyshev-Gauss-Lobatto points when computing nonlinear inviscid fluxes [31]. The stability analysis of SD in previous studies shows the choice of flux point locations is good enough to maintain the stability and the position of solution points has no impact on stability [9]. An example of the positions of flux and solution points for the third-order SD is shown in Fig. 2.

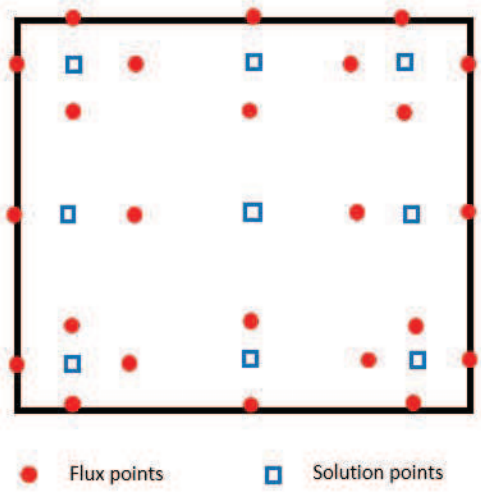

Figure 2: Distribution of flux and solution points for the third order SD scheme.

The conservative variables on the flux points are calculated from the solution points as

$$\begin{aligned}\widetilde{\mathbf{W}}(\xi) &= \sum_{i=1}^{N} \widetilde{\mathbf{W}_{ij}} L_i(\xi) \quad \text{for } \xi \text{ direction,} \\ \widetilde{\mathbf{W}}(\eta) &= \sum_{j=1}^{N} \widetilde{\mathbf{W}_{ij}} L_j(\eta) \quad \text{for } \eta \text{ direction,}\end{aligned} \tag{2.2}$$

where $L_i(\xi), L_j(\eta), i, j = 1, 2, 3, \ldots, N$ are the Lagrange basis functions based on the solution points' locations. N is the order of the SD scheme. And at the interface, the equilibrium state W_0 will be obtained in GKS in the next section. Then, the derivatives of conservative variables on solution points are calculated as follows:

$$\begin{aligned}\left(\frac{\partial \widetilde{\mathbf{W}}}{\partial \xi}\right)_{i,j} &= \sum_{r=0}^{N} \widetilde{\mathbf{W}}_{r+1/2,j} \cdot M'_{r+1/2}(\xi_i), \\ \left(\frac{\partial \widetilde{\mathbf{W}}}{\partial \eta}\right)_{i,j} &= \sum_{r=0}^{N} \widetilde{\mathbf{W}}_{i,r+1/2} \cdot M'_{r+1/2}(\eta_j),\end{aligned} \tag{2.3}$$

where $\widetilde{\mathbf{W}}_{r+1/2,j}$, $\widetilde{\mathbf{W}}_{i,r+1/2}$ are conservative variables on flux points for $r \neq 0, N$ and equilibrium states at interfaces for $r = 0, N$. $M'_{r+1/2}$ is the derivative of the Lagrange basis functions $M_{r+1/2}(\xi), M_{r+1/2}(\eta)$ based on the flux points' locations. Similar to Eq. (2.2), the derivatives of conservative variables on flux points can be obtained. With the conservative variables and their derivatives on flux points, the GKS flux on flux points can be obtained, which will be presented later.

2.2. An example about the SD reconstruction

The third-order SD reconstruction of element i in one-dimension is given as an example. The element i is transformed to the standard interval $[-1,1]$ and the solution points and flux points in this interval are placed at

$$s_1=-\frac{\sqrt{3}}{2},\quad s_2=0,\quad s_3=\frac{\sqrt{3}}{2},$$
$$f_1=-1,\quad f_2=-\frac{\sqrt{3}}{3},\quad f_3=\frac{\sqrt{3}}{3},\quad f_4=1,$$

as shown in the Fig. 3.

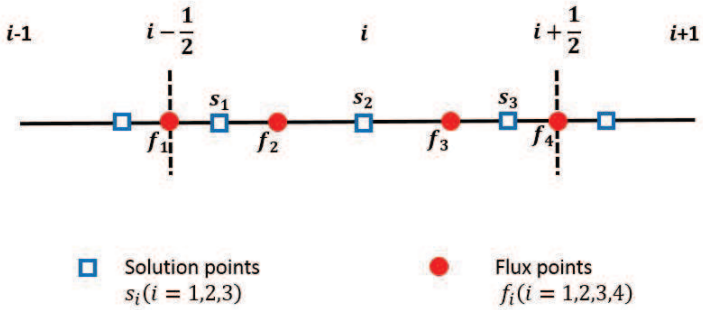

Figure 3: The third-order SD reconstruction in one-dimension for standard element $[-1,1]$.

Then the Lagrangian basis functions for solution and flux points are,

$$L_1(\xi)=\frac{(\xi-s_2)(\xi-s_3)}{(s_1-s_2)(s_1-s_3)},\quad M_1(\xi)=\frac{(\xi-f_2)(\xi-f_3)(\xi-f_4)}{(f_1-f_2)(f_1-f_3)(f_1-f_4)},$$
$$L_2(\xi)=\frac{(\xi-s_1)(\xi-s_3)}{(s_2-s_1)(s_2-s_3)},\quad M_2(\xi)=\frac{(\xi-f_1)(\xi-f_3)(\xi-f_4)}{(f_2-f_1)(f_2-f_3)(f_2-f_4)},$$
$$L_3(\xi)=\frac{(\xi-s_2)(\xi-s_1)}{(s_3-s_2)(s_3-s_1)},\quad M_3(\xi)=\frac{(\xi-f_2)(\xi-f_1)(\xi-f_4)}{(f_3-f_2)(f_3-f_1)(f_3-f_4)},$$
$$M_4(\xi)=\frac{(\xi-f_2)(\xi-f_3)(\xi-f_1)}{(f_4-f_2)(f_4-f_3)(f_4-f_1)}.$$

The conservative variables on solution points, denoted as $\widetilde{\mathbf{W}}_i^s, i=1,2,3$, are known. Then the conservative variables on flux points, denoted as $\widetilde{\mathbf{W}}_i^f, i=1,2,3,4$, can be approximated as Eq. (2.2) by

$$\widetilde{\mathbf{W}}_1^f=L_1(f_1)\widetilde{\mathbf{W}}_1^s+L_2(f_1)\widetilde{\mathbf{W}}_2^s+L_3(f_1)\widetilde{\mathbf{W}}_3^s=\frac{\sqrt{3}+2}{3}\widetilde{\mathbf{W}}_1^s-\frac{1}{3}\widetilde{\mathbf{W}}_2^s+\frac{2-\sqrt{3}}{3}\widetilde{\mathbf{W}}_3^s,$$
$$\widetilde{\mathbf{W}}_2^f=L_1(f_2)\widetilde{\mathbf{W}}_1^s+L_2(f_2)\widetilde{\mathbf{W}}_2^s+L_3(f_2)\widetilde{\mathbf{W}}_3^s=\frac{5}{9}\widetilde{\mathbf{W}}_1^s+\frac{5}{9}\widetilde{\mathbf{W}}_2^s-\frac{1}{9}\widetilde{\mathbf{W}}_3^s,$$

$$\widetilde{\mathbf{W}}_3^f = L_1(f_3)\widetilde{\mathbf{W}}_1^s + L_2(f_3)\widetilde{\mathbf{W}}_2^s + L_3(f_3)\widetilde{\mathbf{W}}_3^s = -\frac{1}{9}\widetilde{\mathbf{W}}_1^s + \frac{5}{9}\widetilde{\mathbf{W}}_2^s + \frac{5}{9}\widetilde{\mathbf{W}}_3^s,$$
$$\widetilde{\mathbf{W}}_4^f = L_1(f_4)\widetilde{\mathbf{W}}_1^s + L_2(f_4)\widetilde{\mathbf{W}}_2^s + L_3(f_4)\widetilde{\mathbf{W}}_3^s = \frac{2-\sqrt{3}}{3}\widetilde{\mathbf{W}}_1^s - \frac{1}{3}\widetilde{\mathbf{W}}_2^s + \frac{\sqrt{3}+2}{3}\widetilde{\mathbf{W}}_3^s.$$

At the boundary $i+1/2$, $\widetilde{\mathbf{W}}_4^f(i)$ from the i-th element reconstruction is considered as the left value, and $\widetilde{\mathbf{W}}_1^f(i+1)$ from the $(i+1)$-th element reconstruction is the right one. Then

$$\widetilde{\mathbf{W}}^f(i+1/2) = \lambda\left(\widetilde{\mathbf{W}}_4^f(i), \widetilde{\mathbf{W}}_1^f(i+1)\right),$$

and similarly,

$$\widetilde{\mathbf{W}}^f(i-1/2) = \lambda\left(\widetilde{\mathbf{W}}_4^f(i-1), \widetilde{\mathbf{W}}_1^f(i)\right),$$

where λ is the collision of left and right equilibrium states regarding GKS solver in the next section. Here for the simplicity, $\widetilde{\mathbf{W}}^f(i+1/2), \widetilde{\mathbf{W}}^f(i-1/2)$ are still denoted as $\widetilde{\mathbf{W}}_4^f, \widetilde{\mathbf{W}}_1^f$ respectively for the i-th element. The derivatives at solution points, denoted as $(\widetilde{\mathbf{W}}_\xi)_i^s$, can be approximated as Eq. (2.3),

$$\begin{aligned}
\left(\widetilde{\mathbf{W}}_\xi\right)_1^s &= M_1'(s_1)\widetilde{\mathbf{W}}_1^f + M_2'(s_1)\widetilde{\mathbf{W}}_2^f + M_3'(s_1)\widetilde{\mathbf{W}}_3^f + M_4'(s_1)\widetilde{\mathbf{W}}_4^f \\
&= -\frac{23+12\sqrt{3}}{16}\widetilde{\mathbf{W}}_1^f + \frac{27\sqrt{3}}{16}\widetilde{\mathbf{W}}_2^f - \frac{3\sqrt{3}}{16}\widetilde{\mathbf{W}}_3^f + \frac{23-12\sqrt{3}}{16}\widetilde{\mathbf{W}}_4^f, \\
\left(\widetilde{\mathbf{W}}_\xi\right)_2^s &= M_1'(s_2)\widetilde{\mathbf{W}}_1^f + M_2'(s_2)\widetilde{\mathbf{W}}_2^f + M_3'(s_2)\widetilde{\mathbf{W}}_3^f + M_4'(s_2)\widetilde{\mathbf{W}}_4^f \\
&= \frac{1}{4}\widetilde{\mathbf{W}}_1^f - \frac{3\sqrt{3}}{4}\widetilde{\mathbf{W}}_2^f + \frac{3\sqrt{3}}{4}\widetilde{\mathbf{W}}_3^f - \frac{1}{4}\widetilde{\mathbf{W}}_4^f, \\
\left(\widetilde{\mathbf{W}}_\xi\right)_3^s &= M_1'(s_3)\widetilde{\mathbf{W}}_1^f + M_2'(s_3)\widetilde{\mathbf{W}}_2^f + M_3'(s_3)\widetilde{\mathbf{W}}_3^f + M_4'(s_3)\widetilde{\mathbf{W}}_4^f \\
&= -\frac{23-12\sqrt{3}}{16}\widetilde{\mathbf{W}}_1^f + \frac{3\sqrt{3}}{16}\widetilde{\mathbf{W}}_2^f - \frac{27\sqrt{3}}{16}\widetilde{\mathbf{W}}_3^f + \frac{23+12\sqrt{3}}{16}\widetilde{\mathbf{W}}_4^f.
\end{aligned}$$

2.3. Gas-kinetic solver

The two-dimensional BGK equation [3] is given as

$$f_t + uf_x + vf_y = \frac{g-f}{\tau}, \tag{2.4}$$

where $\mathbf{u} = (u, v)$ is the particle velocity, f is the distribution function, g is the Maxwellian distribution and τ is the collision time. The collision term satisfies the compatibility condition

$$\int \frac{g-f}{\tau}\psi \mathrm{d}\Xi = 0, \tag{2.5}$$

where

$$\psi = (\psi_1, \ldots, \psi_4)^T = \left(1, u, v, \frac{1}{2}\left(u^2+v^2+\zeta^2\right)\right)^T$$

and ζ is the internal variables related to the internal degree of freedom.

In the smooth region, the gas distribution function can be expanded as

$$f = g - \tau D_{\mathbf{u}} g + \tau D_{\mathbf{u}} (\tau D_{\mathbf{u}}) g - \tau D_{\mathbf{u}} [\tau D_{\mathbf{u}} (\tau D_{\mathbf{u}}) g] + \cdots,$$

where $D_{\mathbf{u}} = \partial/\partial t + \mathbf{u} \cdot \nabla$. With the zeroth-order truncation f = g, the Euler equations can be obtained. For the first-order truncation

$$f = g - \tau(u g_x + v g_y),$$

the Navier-Stokes equations can be obtained.

To update the flow variables, the flux is based on the integral solution of Eq. (2.4) [33]

$$f(\mathbf{x}_i, t, \mathbf{u}, \zeta) = \frac{1}{\tau} \int_0^t g\left(\mathbf{x}', t', \mathbf{u}, \zeta\right) e^{-\left(t-t'\right)/\tau} dt' + e^{-t/\tau} f_0(-\mathbf{u}t, \mathbf{u}, \zeta),$$

where $\mathbf{x}_i = 0$ is the location of the node point. Based on it, a second-order time-dependent gas distribution function $f(\mathbf{x}_i, t, \mathbf{u}, \zeta)$ can be obtained [33], viz.

$$\begin{aligned} f(\mathbf{x}_i, t, \mathbf{u}, \zeta) = {} & \left(1 - e^{-t/\tau_n}\right) g_0 + \left[(t+\tau) e^{-t/\tau_n} - \tau\right] (\overline{a}_1 u + \overline{a}_2 v) g_0 + \left(t - \tau + \tau e^{-t/\tau_n}\right) \overline{A} g_0 \\ & + e^{-t/\tau_n} g_r \left[1 - (\tau + t)(a_{1r} u + a_{2r} v) - \tau A_r\right] \left(1 - H(u)\right) \\ & + e^{-t/\tau_n} g_l \left[1 - (\tau + t)(a_{1l} u + a_{2l} v) - \tau A_l\right] H(u). \end{aligned} \tag{2.6}$$

Through the spatial reconstruction of macroscopic flow variables in the SD method, the conservative variables W_l and W_r on the left- and right-hand sides of a cell interface flux point, and the corresponding equilibrium states g_l and g_r can be determined. And thus by the compatibility condition (2.5), the conservative variables W_0 and the equilibrium state g_0 at the cell interface can be obtained as follows:

$$\int \psi g_0 \mathrm{d}\Xi = W_0 = \int_{u>0} \psi g_l \mathrm{d}\Xi + \int_{u<0} \psi g_r \mathrm{d}\Xi. \tag{2.7}$$

The spatial derivatives of the left and right states in both normal and tangential directions, such as a_{il}, a_{ir} $(i = 1, 2)$, are determined by the normal and tangential derivatives of the initial macroscopic flow variables [21]. The time derivatives A_l, A_r can be obtained from the requirement on the first-order Chapman-Enskog expansion such as

$$\int g_l (a_{1l} u + a_{2l} v + A_l) \psi \mathrm{d}\Xi = 0, \quad \int g_r (a_{1r} u + a_{2r} v + A_r) \psi \mathrm{d}\Xi = 0.$$

With the determination of gas distribution function in Eq. (2.6), the fluxes in x- and y-direction of macroscopic variables can be evaluated as

$$F = \int u f \psi \mathrm{d}\Xi, \quad G = \int v f \psi \mathrm{d}\Xi. \tag{2.8}$$

Similarly, the spatial and temporal derivatives in the equilibrium state are obtained by

$$\int \overline{a}_1 \psi g_0 \mathrm{d}\Xi = \frac{\partial \overline{W}}{\partial x}, \quad \int \overline{a}_2 \psi g_0 \mathrm{d}\Xi = \frac{\partial \overline{W}}{\partial y}, \quad \int (\overline{a}_1 u + \overline{a}_2 v + \overline{A}) \psi g_0 \mathrm{d}\Xi = 0. \tag{2.9}$$

In a well-resolved region with continuous flow distributions, i.e., at the flux points inside a cell, the time-dependent gas distribution function in Eq. (2.6) is reduced to

$$f(x_i, t, u, v, \zeta) = g\big(1 - \tau(\bar{a}_1 u + \bar{a}_2 v + \bar{A}) + \bar{A}t\big). \tag{2.10}$$

For the Euler solution $\tau = 0$, it is simplified as

$$f\,(x_i, t, u, v, \xi) = g(1 + \bar{A}t). \tag{2.11}$$

2.4. Two-stage fourth-order discretization

The high-order time stepping method is adopted for the above time evolution solution. The two-stage fourth-order scheme [21] is used in SDGKS. For time-dependent equation,

$$\frac{\mathrm{d}\widetilde{\mathbf{W}}_{ij}}{\mathrm{d}t} = -\left(\frac{\partial \widetilde{\mathbf{F}}}{\partial \xi}\right)_{i,j} - \left(\frac{\partial \widetilde{\mathbf{G}}}{\partial \eta}\right)_{i,j} := \mathscr{L}\left(\widetilde{\mathbf{W}}_{ij}\right),$$

where $\mathscr{L}$ is an operator for spatial discretization. It is computed at the solution point (i, j) by using the derivatives of Lagrange operators $M'_{r+1/2}$ in Eq. (2.3),

$$\left(\frac{\partial \widetilde{\mathbf{F}}}{\partial \xi}\right)_{i,j} = \sum_{r=0}^{N} \widetilde{\mathbf{F}}_{r+1/2,j} \cdot M'_{r+1/2}(\xi_i),$$
$$\left(\frac{\partial \widetilde{\mathbf{G}}}{\partial \eta}\right)_{i,j} = \sum_{r=0}^{N} \widetilde{\mathbf{G}}_{i,r+1/2} \cdot M'_{r+1/2}(\eta_j).$$

Then, a fourth-order temporal accurate solution for $\widetilde{\mathbf{W}}(t)$ at $t = t_n + \Delta t$ can be obtained by

$$\widetilde{\mathbf{W}}^* = \widetilde{\mathbf{W}}^n + \frac{1}{2}\Delta t \mathscr{L}\left(\widetilde{\mathbf{W}}^n\right) + \frac{1}{8}\Delta t^2 \frac{\partial}{\partial t}\mathscr{L}\left(\widetilde{\mathbf{W}}^n\right), \tag{2.12}$$
$$\widetilde{\mathbf{W}}^{n+1} = \widetilde{\mathbf{W}}^n + \Delta t \mathscr{L}\left(\widetilde{\mathbf{W}}^n\right) + \frac{1}{6}\Delta t^2 \left(\frac{\partial}{\partial t}\mathscr{L}\left(\widetilde{\mathbf{W}}^n\right) + 2\frac{\partial}{\partial t}\mathscr{L}\left(\widetilde{\mathbf{W}}^*\right)\right), \tag{2.13}$$

where $\mathscr{L}$ and $(\partial/\partial t)\mathscr{L}$ are related to the fluxes and the time derivatives of the fluxes evaluated from the time-dependent gas distribution function $f(t)$ at the flux points. The details can be found in [21].

2.5. Procedure of SDGKS

In this section, the procedure of SDGKS is summarized. The subscript f refers to the flux points, subscript s refers to the solution points, and subscript c stands for cell index. The superscripts $l, r, 0$ stand for the left, right, and center equilibrium states.

- Reconstruct $W_{f,c}$ from the conservative variables $W_{s,c}$ using Eq. (2.2).
- Obtain the equilibrium state $W^0_{f,c}$ on the element interfaces as Eq. (2.7). Meanwhile, boundary conditions shall be applied.
- Evaluate $\nabla W_{s,c}$ from $W^0_{f,c}$ on the element interfaces and $W_{f,c}$ inside the element by Eq. (2.3), where

$$\nabla W = \left\{ \begin{array}{c} W_x \\ W_y \end{array} \right\} \quad \text{and} \quad W_x = \frac{\partial W}{\partial \xi}\xi_x + \frac{\partial W}{\partial \eta}\eta_x,$$

  etc.
- Reconstruct $\nabla W_{f,c}$ from Eq. (2.2), get the derivatives of equilibrium states by Eq. (2.7) and Eq. (2.9) on the element interfaces.
- Use $W^{l,r,0}_{f,c}$ and $\nabla W^{l,r,0}_{f,c}$ to compute the gas distribution function in Eq. (2.6) and get the fluxes in Eq. (2.8) on the element interfaces. Use $W_{f,c}$ and $\nabla W_{f,c}$ inside the element to compute the smooth flux by taking moments of Eq. (2.10) or Eq. (2.11).
- Update the conservative variables by two-stage fourth-order time stepping, i.e. Eq. (2.12) and Eq. (2.13).

3. Linear Stability Analysis

Linear stability for the full discretization (space and time) is performed in the present study. The second-order to fourth-order SDGKS using one stage second order (S1O2) and two stages fourth order (S2O4) are studied. And the traditional spectral difference method using Riemann solver, such as Rusanov solver, with the simple Euler forward and the fourth-order strong stability preserving Runge-Kutta time stepping scheme is also presented as the comparison.

Following the approach described in Van den Abeele *et al.* [31], we consider the 1D advection equation

$$\frac{\partial u}{\partial t} + a\frac{\partial u}{\partial x} = 0, \tag{3.1}$$

$a > 0$ in 1D uniform mesh. The generating pattern is trivial since it consists of one cell, defined by its size Δx. Discretizing (3.1) in space with the SD method on the mesh and in time with the explicit one-step time marching strategy yields an expression of the following form:

$$\mathbf{u}_i{}^{n+1} = \mathbf{u}_i^n + \frac{a\Delta t}{\Delta x}\mathbf{A}_i$$

for Riemann flux, and

$$\mathbf{u}_i{}^{n+1} = \mathbf{u}_i^n + \frac{a\Delta t}{\Delta x}\mathbf{A}_i + \frac{a^2\Delta t^2}{2\Delta x^2}\mathbf{B}_i$$

for GKS flux, where

$$\begin{aligned}\mathbf{A}_i &= -\mathbf{D}\left(\mathbf{M}^{-1}\mathbf{u}_{i-1} + \mathbf{M}^0\mathbf{u}_i + \mathbf{M}^{+1}\mathbf{u}_{i+1}\right),\\ \mathbf{B}_i &= -\mathbf{D}\left(\mathbf{M}^{-1}\mathbf{A}_{i-1} + \mathbf{M}^0\mathbf{A}_i + \mathbf{M}^{+1}\mathbf{A}_{i+1}\right).\end{aligned}$$

The Matrices $\mathbf{M}^{-1}$, $\mathbf{M}^0$ and $\mathbf{M}^1$ represent the extrapolation of the solution to the flux points, and the matrix $\mathbf{D}$ is for the computation of the flux derivatives at the solution points. The detailed computations of those matrices have been elaborated in [1,12,17]. $\mathbf{u}_i$ is a column vector containing the solution at all the solution points in the cell with index i.

3.1. Riemann flux with fourth-order SSP Runge-Kutta scheme

The Rusanov solver [27] is used at the cell interface

$$\mathbf{F} = \frac{1}{2}\left[\left(\mathbf{F}(U_L) + \mathbf{F}(U_R)\right)\cdot\mathbf{n} - \lambda_{\max}(U_R - U_L)\right],$$

where $\lambda_{\max}$ is the absolute value of maximum characteristic speed. The flux is simplified to the upwind flux in the linear advection equation,

$$\mathbf{F}(t) = \mathbf{F}(U_L, t) = aU_L.$$

With explicit RK time stepping methods, solution $\mathbf{u}^{n+1}$ is obtained from $\mathbf{u}^n$ as

$$\begin{aligned}&\mathbf{w}^{(0)} = \mathbf{u}^n,\\ &\mathbf{w}^{(k)} = \sum_{l=0}^{k-1}\alpha_{kl}\mathbf{w}^{(l)} + \nu\beta_{kl}\mathbf{A}\mathbf{w}^{(l)}, \quad k = 1,2,\ldots,p,\\ &\mathbf{u}^{n+1} = \mathbf{w}^{(p)},\end{aligned}$$

where $\nu = (a\Delta t)/\Delta x$ is the Courant-Friedrichs-Lewy (CFL) number. For the SSP method used in [9], $p = 5$ is the stage number, α and β are given by

$$\alpha = \begin{bmatrix} 1 & & & & & \\ 0.444370494067 & 0.555629505932 & & & & \\ 0.620101851385 & 0 & 0.379898148615 & & & \\ 0.178079954108 & 0 & 0 & 0.821920045892 & & \\ 0.006833258840 & 0 & 0.517231672090 & 0.127598311333 & 0.348336757737 & \end{bmatrix},$$

$$\beta = \begin{bmatrix} 0.391752227004 & & & & & \\ 0 & 0.368410592630 & & & & \\ 0 & 0 & 0.251891774247 & & & \\ 0 & 0 & 0 & 0.544974750212 & & \\ 0 & 0 & 0 & 0.084604163382 & 0.226007483194 & \end{bmatrix}.$$

And the amplification matrix can be obtained by

$$\begin{aligned}\mathbf{G}^{(0)} &= \mathbf{I},\\ \mathbf{G}^{(k)} &= \sum_{l=0}^{k-1}(\alpha_{kl}\mathbf{I}+\nu\beta_{kl}\mathbf{A})\mathbf{G}^{(l)}, \quad k=1,2,\ldots,p.\end{aligned} \tag{3.2}$$

For the sspRK5O4, $\mathbf{G}^{(5)}$ is the amplification matrix and its spectral radius should always be smaller than one, i.e. $|\lambda(\nu,\theta)| \leq 1$. It is hard to get the analytic solution for high-order schemes. Instead, we numerically compute the solution set

$$|\lambda_{i,k}| = |\lambda(\nu_i,\theta_k)|, \quad 0<\nu_i<4, \quad 0<\theta_k<2\pi.$$

And the contour line with $|\lambda_{i,k}|=1$ is plotted. The minimum ν on it is the CFL condition. The stability regions of the Rusanov solver combined with simple Euler forward (RK1) and the five-stage fourth-order SSP Runge-Kutta (sspRK5O4) are shown in Fig. 4. It is obvious that, for the same order of spatial discretization, the CFL number is much larger for sspRK5O4 than that for the RK1 scheme, indicating the time marching method plays an important role in the stability.

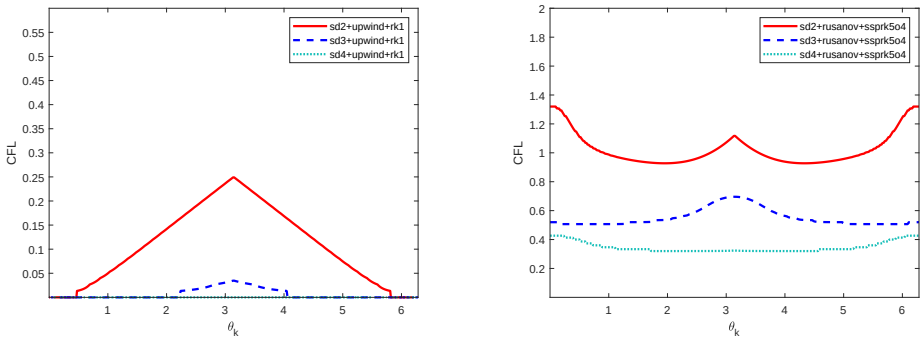

(a) Rusanov flux with RK1 (b) Rusanov flux with sspRK5O4

Figure 4: The stability contours of different SD schemes with Rusanov flux for solving the scalar linear advection equation.

3.2. GKS flux with S1O2, S2O4 and sspRK5O4

The equilibrium state U_0 in the GKS solver is determined by

$$\begin{aligned}U_0 &= \langle U_L\rangle_{u>0} + \langle U_R\rangle_{u<0}\\ &= \big(1/2\mathrm{erfc}(-\sqrt{\lambda}c)\big)U_L + \big(1/2\mathrm{erfc}(\sqrt{\lambda}c)\big)U_R\\ &\approx 0.84U_L + 0.16U_R,\end{aligned}$$

where $\lambda = 1/2, c = 1$ for the scalar linear advection equation. And the smooth flux of second-order time accuracy turns out to be

$$F(t) = F(U_0,t) = aU_0 - a^2U_{0x}t.$$

The flux of first-order time accuracy is simplified as

$$F(t) = F(U_0, t) = aU_0.$$

As a result, the matrices $\mathbf{M}^{-1}$, $\mathbf{M}^0$ and $\mathbf{M}^1$ when using GKS flux are slightly different from them when Riemann flux is used in (3.1).

The amplification matrix $\mathbf{G}^{(5)}$ for first-order GKS flux and sspRK5O4 can be obtained by the same formula in Eq. (3.2). The amplification matrix $\mathbf{G}^{(1)}$ for S1O2 can be obtained,

$$\mathbf{G}^{(1)} = \mathbf{I} + \nu\mathbf{A} + \frac{1}{2}\nu^2\mathbf{B}.$$

The amplification matrix $\mathbf{G}^{(2)}$ for S2O4 is

$$\mathbf{G}^{(1)} = \mathbf{I} + \frac{1}{2}\nu\mathbf{A} + \frac{1}{8}\nu^2\mathbf{B},$$
$$\mathbf{G}^{(2)} = \mathbf{I} + \nu\mathbf{A} + \frac{1}{6}\nu^2\mathbf{B} + \frac{1}{3}\nu^2\mathbf{B}\mathbf{G}^{(1)}.$$

The stability regions of different time stepping schemes when using GKS solver are illustrated in Fig. 5. It shows the SDGKS is linearly stable. The approximate CFL numbers

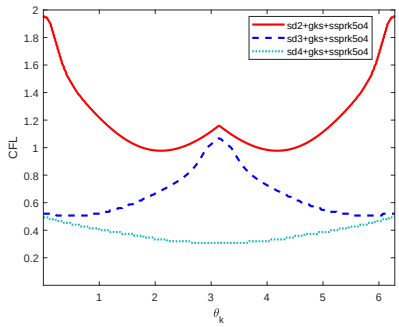

(a) 1st GKS with sspRK5O4

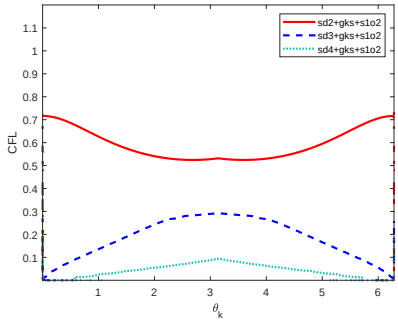

(b) 2nd GKS with S1O2

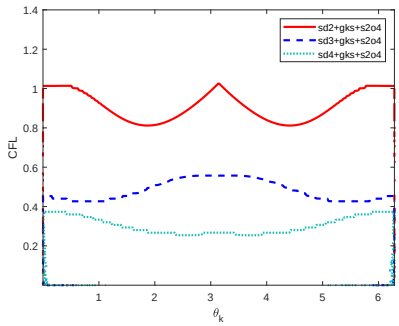

(c) 2nd GKS with S2O4

Figure 5: The stability contours of SDGKS for solving the scalar linear advection equation.

Table 1: The theoretical maximum CFL numbers of different schemes for linear advection equation.

Order	Rusanov+sspRK5O4	GKS+sspRK5O4	GKS+S2O4
Second-order SD	0.92	0.96	0.82
Third-order SD	0.51	0.51	0.43
Fourth-order SD	0.32	0.31	0.26

of different schemes are shown in Table 1. Although the CFL number for GKS+S2O4 is a bit smaller than the traditional one, it is more efficient with fewer stages. In addition, all the numerical schemes become more stable when the time stepping accuracy is matched with the spatial accuracy, and the CFL number is larger when more stages are used for time-discretization.

4. Numerical Tests

In this section, the numerical tests will be presented to validate the high-order SDGKS. The collision time in the inviscid GKS flux is defined as [33],

$$\tau_n = C_1\Delta t + C_2\left|\frac{p_l - p_r}{p_l + p_r}\right|\Delta t$$

with $C_1 = 0.05$ and $C_2 = 1$. For viscous flows, the collision time is related to the viscosity coefficient,

$$\tau_n = \frac{\mu}{p} + C_2\left|\frac{p_l - p_r}{p_l + p_r}\right|\Delta t,$$

where p_l and p_r denote the pressures on the left and right sides of the cell interface, μ is the dynamic viscosity coefficient. In the smooth region, $\tau = \mu/p$. In the following tests, the smooth flux equation (2.10) will be adopted on the flux points inside the cell and the full flux equation (2.6) will be used at the cell boundaries unless it is specified. The S2O4 time stepping method is used in high-order SDGKS simulations, and the S1O2 time stepping method [8] is used for the second-order SDGKS. The specific heat ratio takes $\gamma = 1.4$. The CFL number is set as $0.1 \sim 0.6$ for the present cases.

4.1. Accuracy test

The order of accuracy of SDGKS is tested by the 2D density perturbation. The initial condition and analytic solutions are given as follows:

$$\rho(x,y) = 1+0.2\sin\big(\pi(x+y)\big), \quad U(x,y) = 1, \quad V(x,y) = 1, \quad p(x,y) = 1, \quad x,y \in [0,2].$$

And the smooth flux is used at the element boundaries. The errors and convergence orders are shown in Table 2. The designed order of accuracy is achieved. The results of traditional SDRus schemes are presented in Table 3 as reference. From the tables, it is clear that SDGKS usually has smaller errors compared with SDRus in the simulations.

Table 2: Error and convergence order for 2D sin-wave propagation for SDGKS with S2O4.

Mesh	L^1 error	Order	L^2 error	Order	L^∞ error	Order
Second-order SD						
10^2	2.34e-2	-	2.59e-2	-	3.87e-2	-
20^2	6.68e-3	1.84	7.50e-3	1.82	1.24e-2	1.81
40^2	1.71e-3	1.94	1.91e-3	1.95	2.91e-3	1.95
80^2	4.33e-4	1.98	4.83e-4	1.98	7.52e-4	1.95
160^2	1.09e-4	1.99	1.21e-4	1.99	1.88e-4	2.00
Third-order SD						
10^2	3.92e-4	-	4.73e-4	-	1.28e-3	-
20^2	4.54e-5	2.99	5.92e-5	2.99	1.77e-4	2.86
40^2	5.70e-6	2.99	7.57e-6	2.97	2.28e-5	2.95
80^2	7.18e-7	2.99	9.65e-7	2.97	2.93e-6	2.96
160^2	9.06e-8	2.98	1.22e-7	2.98	3.71e-7	2.98
Fourth-order SD						
10^2	1.97e-5	-	2.66e-5	-	8.63e-5	-
20^2	1.30e-6	3.92	1.74e-6	3.93	5.79e-6	3.90
40^2	8.32e-8	3.97	1.12e-7	3.96	3.73e-7	3.96
80^2	5.26e-9	3.98	7.14e-9	3.98	2.38e-8	3.97
160^2	3.30e-10	3.99	4.49e-10	3.99	1.51e-9	3.98

Table 3: Error and convergence order for 2D sin-wave propagation for SDRus with sspRK5O4.

Mesh	L^1 error	Order	L^2 error	Order	L^∞ error	Order
Second-order SD						
10^2	2.62e-2	-	2.99e-2	-	4.17e-2	-
20^2	6.65e-3	1.97	7.36e-3	2.02	1.06e-2	1.96
40^2	1.61e-3	2.03	1.79e-3	2.03	2.59e-3	2.03
80^2	3.74e-4	2.11	4.15e-4	2.11	5.96e-4	2.12
160^2	6.38e-5	2.55	7.08e-5	2.55	1.02e-4	2.54
Third-order SD						
10^2	5.14e-4	-	6.83e-4	-	1.68e-3	-
20^2	8.14e-5	2.66	1.08e-4	2.65	2.79e-4	2.59
40^2	1.11e-5	2.87	1.49e-5	2.86	3.88e-5	2.84
80^2	1.42e-6	2.95	1.92e-6	2.95	5.02e-6	2.94
160^2	1.80e-7	2.98	2.43e-7	2.98	6.35e-7	2.98
Fourth-order SD						
10^2	2.90e-5	-	3.33e-5	-	7.85e-5	-
20^2	1.72e-6	4.07	1.96e-6	4.08	4.79e-6	4.03
40^2	1.06e-7	4.02	1.21e-7	4.02	2.96e-7	4.01
80^2	6.52e-9	4.02	7.48e-9	4.02	1.88e-8	3.97
160^2	4.56e-10	3.83	5.58e-10	3.74	1.55e-9	3.60

4.2. Double shear flow

The double shear flow is a canonical test problem for a scheme's accuracy and resolution in incompressible flows. A comparison has been done by Minion *et al.* [18] for the solution under different resolution. The initial flow is set as

$$
\begin{aligned}
U(x,y) &= \begin{cases} \tanh\big(k(y-0.25)\big), & y \le 0.5, \\ \tanh\big(k(0.75-y)\big), & y > 0.5, \end{cases} \\
V(x,y) &= \delta \sin(2\pi x), \\
\rho(x,y) &= p(x,y) = 1,
\end{aligned}
$$

where $k = 100$ and $\delta = 0.05$. The kinetic viscosity is $\nu = 5.0 \cdot 10^{-5}$. The periodic boundary condition is adopted in both x and y directions. The vorticity contours of high-order SDGKS and Rusanov are shown in Fig. 6. The resolution of high-order SDGKS is slightly better than that from high-order Rusanov flux with sspRK5O4.

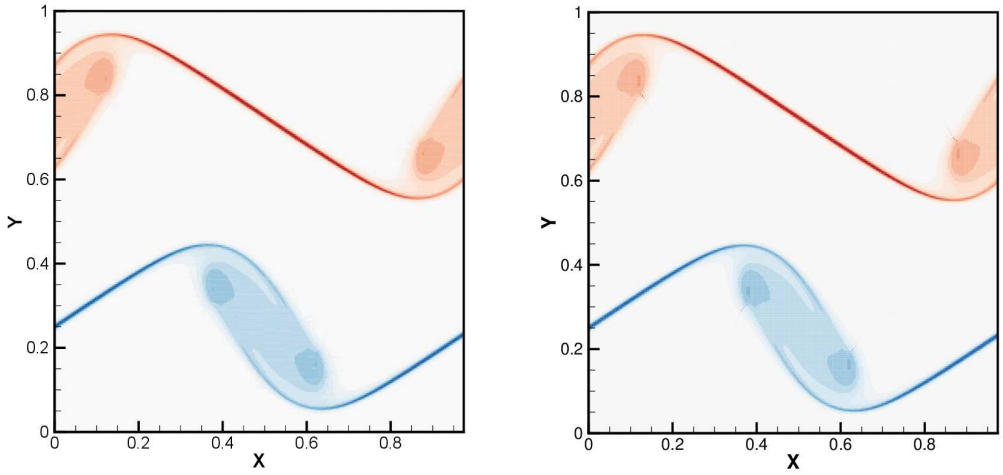

Figure 6: Double shear flow vorticity contours using SD4 at $t = 1.2$. Left: Rusanov flux + RK5; Right: GKS + S2O4.

4.3. Laminar boundary layer

A low-speed laminar boundary layer with incoming Mach number $Ma = 0.15$ is simulated over a flat plate with Reynolds number $Re = U^{\infty} L/\mu = 10^5$, where $L = 100$ is the characteristic length. The computational domain is shown in Fig. 7, where the flat plate is placed at $x > 0$ and $y = 0$. Total $120 * 35$ mesh points are used in the domain with a refined cell size $h = 0.05$ close to the boundary. There are 40 mesh points in the front of the plate. The adiabatic non-slip boundary condition is imposed on the plate and the symmetric slip boundary condition is set at the bottom boundary in the front of the plate. The non-reflecting boundary condition based on the Riemann invariants is adopted for the other

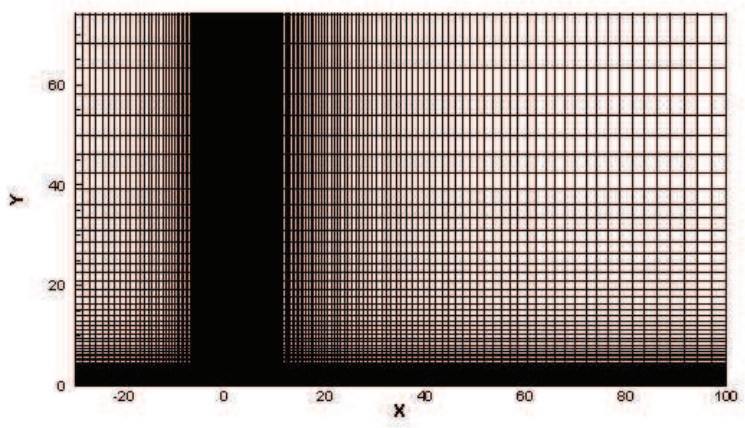

Figure 7: Non-uniform mesh in the computational domain for laminar boundary layer $[-30,100]*[0,80]$.

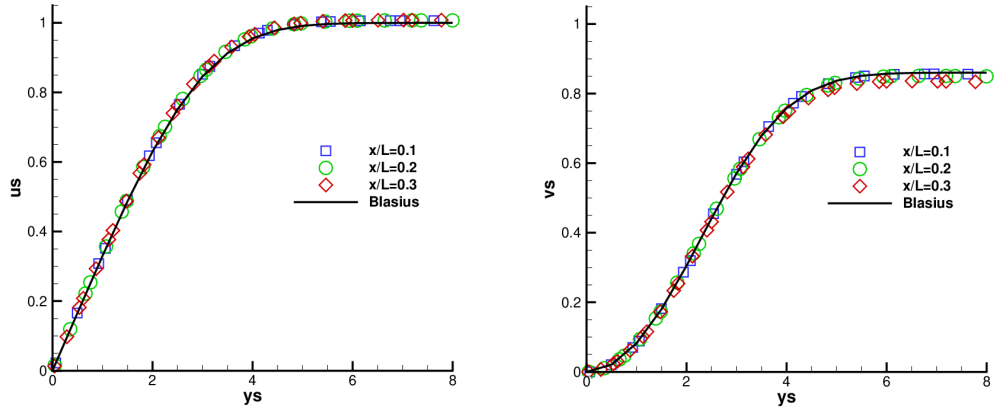

Figure 8: Laminar boundary layer: the non-dimensional velocities by SD3GKS compared with the Blasius reference. $Re = 10^5, Ma = 0.15$.

boundaries, where the free stream is set as $\rho^\infty = 1, p^\infty = 1/\gamma$. The non-dimensional velocity U and V are given in Fig. 8 at three selected locations $x/L = 0.1, 0.2, 0.3$. The numerical results match well with the analytical solutions.

4.4. Inviscid flow around NACA0012 airfoil

The exact formula defining the geometry of NACA0012 airfoil is

$$y = \pm 0.6 \times \left(0.29690x^{0.5} - 0.12600x - 0.35160x^2 + 0.28430x^3 - 0.10150x^4\right). \quad (4.1)$$

The unstructured quadrilateral mesh is shown in Fig. 9(a) and there are in total 2856 elements in a circular computational domain with a radius of 20. The Mach number is 0.63 and the angle of attack $\theta_a = 2^\circ$. The SD2GKS and SD4GKS are used in this case. Third-order

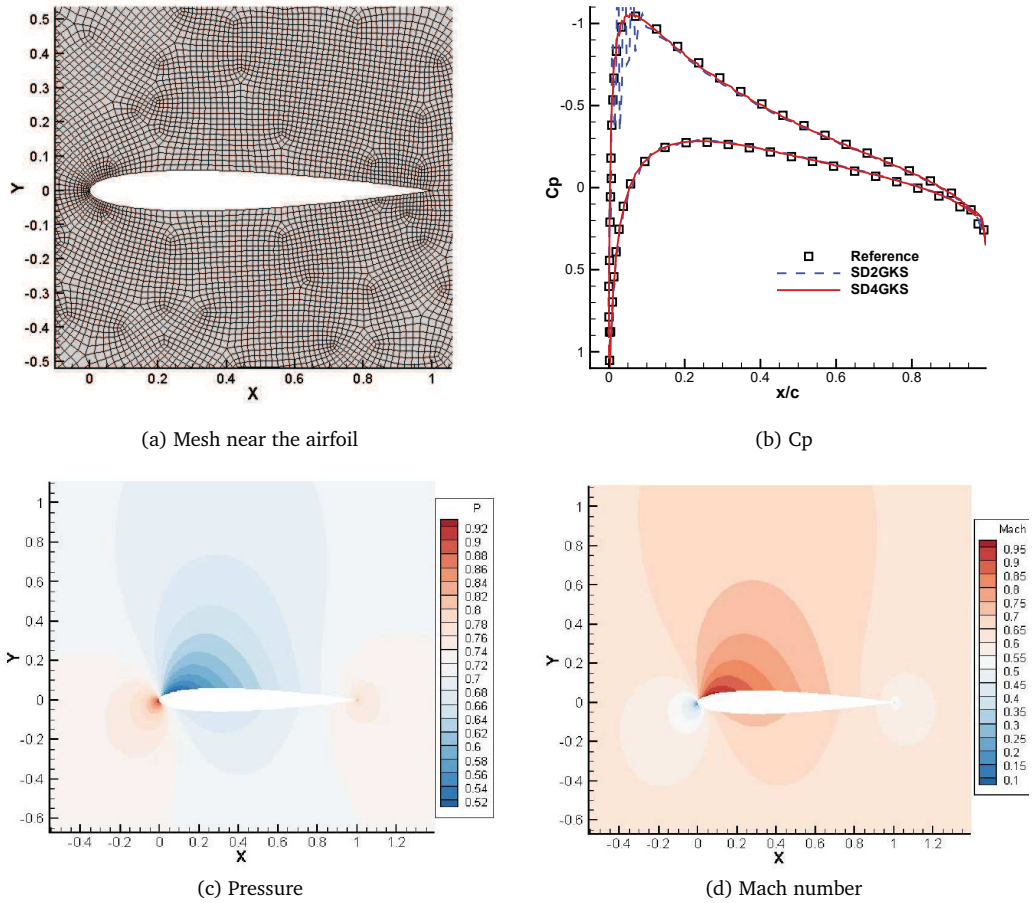

(a) Mesh near the airfoil

(b) Cp

(c) Pressure

(d) Mach number

Figure 9: Inviscid flow past the NACA0012, $Ma = 0.63$, $\theta_a = 2°$, SD4GKS.

elements were used on the surface of the airfoil. The pressure coefficients on the surface of the airfoil are plotted in Fig. 9(b). There are some oscillations in the numerical result from second-order SD2GKS due to the low order reconstruction, while the solution from high-order SD4GKS agrees well with the reference [9]. The results indicate the necessary to use high-order method on such a coarse mesh. The pressure and Mach number contours are shown in Figs. 9(c)-9(d). The results show that the current method works well for this case on the unstructured mesh.

4.5. Viscous flow around a cylinder

The viscous flow past a cylinder at Reynolds numbers of 40 and 100 have been studied. The curvilinear mesh of 12480 cells in the circular domain with the radius of 100, is used in this case, and the near wall size $h \approx 1/40$. The nonreflecting boundary condition is applied and the third-order elements were used on the surface of the cylinder.

4.5.1. Reynolds number 40

The contours of velocities and pressure are shown in Fig. 10. The streamlines of velocity around a cylinder are presented in Fig. 11. And the drag coefficient along with the computational time for SD3GKS is shown in Fig. 12. In Table 4, the drag coefficient Cd, wake length Lw, vortex height Hv, vortex width Wv, and separation angle θ_s obtained by SDGKS are compared with those by experiments and other methods. The results agree well with the reference data.

Table 4: The result comparison for steady flow passing through a circular cylinder.

	Cd	Lw	Hv	Wv	θ_s
Experiment [30]	1.46-1.56	-	-	-	-
Experiment [6]	-	2.12	0.297	0.751	53.5°
DDG [37]	1.529	2.31	-	-	-
p-multigrid CGKS [7]	1.525	2.22	0.296	0.714	53.5°
Current SD3GKS	1.524	2.26	0.296	0.717	53.6°

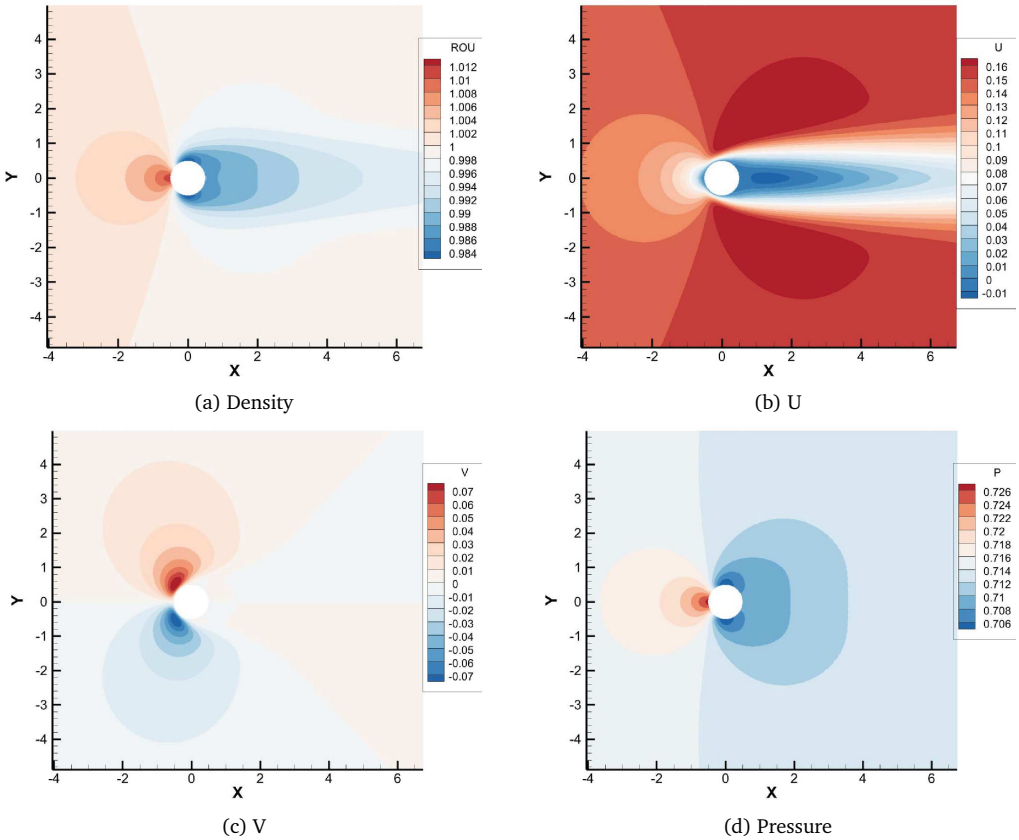

(a) Density (b) U

(c) V (d) Pressure

Figure 10: Viscous flow past the cylinder, $Re = 40, Ma = 0.15$, by SD3GKS.

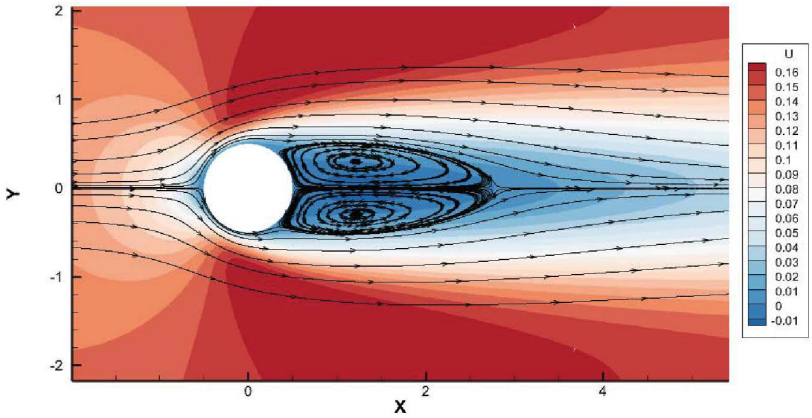

Figure 11: Velocity streamlines around a cylinder at $Re = 40$ by SD3GKS.

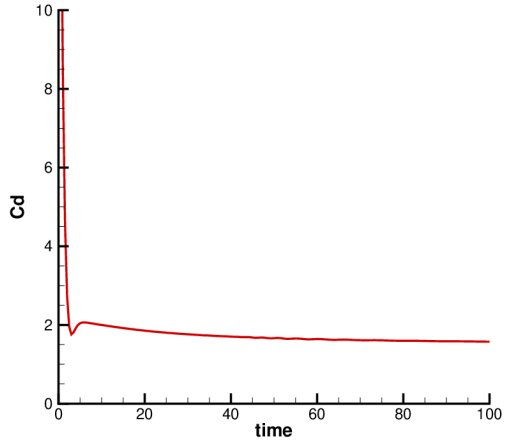

Figure 12: Drag coefficient against time at $Re = 40$ by SD3GKS.

4.5.2. Reynolds number 100

The flow past a cylinder with Reynolds number 100 is also investigated by SD2GKS and SD3GKS. Figs. 13 and 14 show the vorticity behind the cylinder. The high-order scheme presents higher resolution solution than that from second-order scheme on the same coarse mesh. And the lift coefficient against computational time is presented in Fig. 15. Root-mean-square (RMS) values are used to present the fluctuating lift coefficient, $Cl_{RMS} = \sqrt{\sum_{i=1}^{N}(Cl_i - Cl_{mean})^2/N}$, where Cl_i is the value at an instant and Cl_{mean} is the mean value from N points. All those numbers are in a single vortex shedding cycle. The RMS lift coefficient, the pressure, and viscous lift coefficient $Cl_{RMS}, Cl_{RMS}(p), Cl_{RMS}(v)$, and the Strouhal number obtained by the current study and reference results are shown in Table 5. The results of the current study match with those of other references in which finer meshes are used in the simulation. For example, there are in total 14441 cells in the study of Sharman et al [28]. It shows that the current method is quite accurate and efficient.

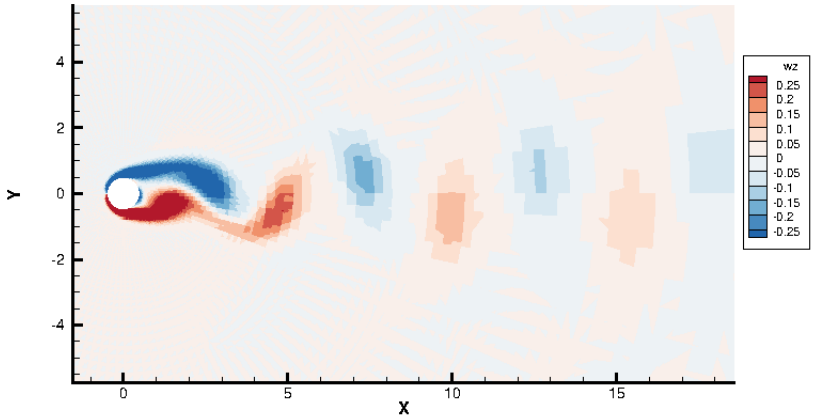

Figure 13: Vorticity contour around a cylinder at $Re = 100$ by SD2GKS.

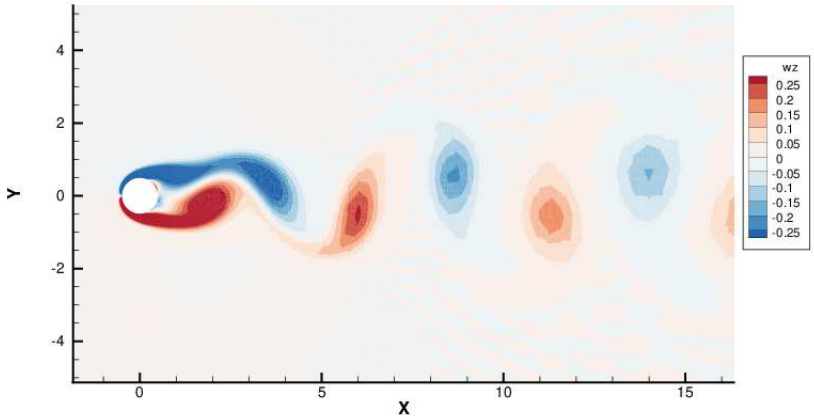

Figure 14: Vorticity contour around a cylinder at $Re = 100$ by SD3GKS.

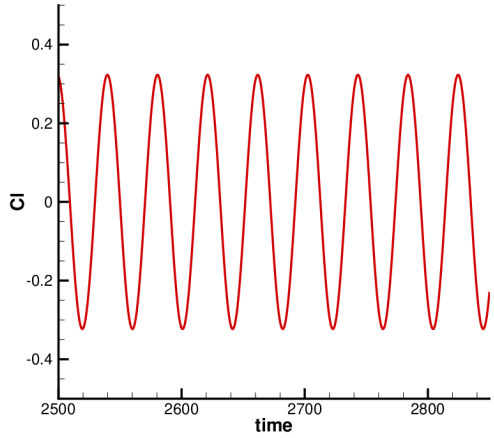

Figure 15: The lift coefficient against time at $Re = 100$ by SD3GKS.

Table 5: The RMS lift coefficient in comparison with the benchmark solutions for flow over a cylinder at $Re = 100$.

	Park *et al.* [22]	Sharman *et al.* [28]	Li *et al.* [9]	Current work
Strouhal number	0.165	0.164	0.166	0.166
Cl_{RMS}	0.23	0.23	0.23	0.23
$Cl_{RMS}(v)$	0.03	0.03	0.03	0.03
$Cl_{RMS}(p)$	0.21	0.20	0.20	0.20

4.6. CPU time comparison

SDGKS can use almost the same CFL number as the spectral difference scheme of Rusanov flux and sspRK5O4 (SDRus) time stepping method. They have the similar values for time step Δt in simulation. In order to find out the efficiency from the current scheme, two comparisons regarding the CPU time have been investigated. The initial and boundary conditions are set as the accuracy tests of fourth-order SD in Section 4.1 for both inviscid and viscous tests. And the smooth flux is used at the element boundaries for GKS solver. For the viscous one, the same code is used by setting the coefficient $\nu = 0$.

In the first comparison, the CPU time (s) is recorded for every 1000 steps by using two schemes on the 2D mesh with 10^2 cells. The results are shown in Table 6. It shows that the SDRus costs just half time for inviscid cases compared with SDGKS, since it is a flux solver of first-order time accuracy and the reconstruction of derivatives is omitted. However, for viscous cases, SDGKS-S2O4 saves 8% of CPU time every 1000 steps.

Secondly, the overall efficiency in the sin-wave propagation is tested. The fourth-order schemes in both space and time are used for SDGKS and SDRus. The CPU time (s) and the errors of the numerical solutions compared with the analytical solution on mesh $10^2, 20^2, 40^2, 80^2$ are recorded as well. The results are shown in Fig. 16. It is clear that SDGKS is more efficient than SDRus in viscous flows.

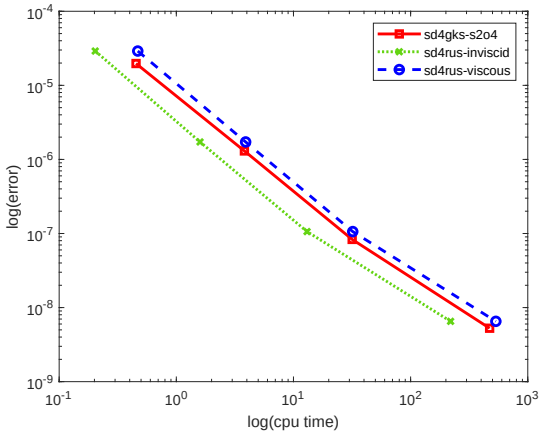

Figure 16: The L^1 errors against the CPU time (s) for two schemes.

Table 6: The comparison of two schemes about the CPU time (s) of every 1000 steps.

	SDRus	SDGKS
inviscid	1.5508	3.4375
viscous	3.7305	3.4375

5. Conclusion and Future Work

In this paper, the high-order spectral difference gas-kinetic schemes (SDGKS) are successfully developed on the unstructured quadrilateral meshes. Instead of the traditional Riemann solver with Runge-Kutta time stepping, the two-stage fourth-order time stepping method is adopted in SDGKS. The efficiency test shows that the SDGKS is more efficient than the traditional SD method. The stability of SDGKS was analyzed for the linear advection equation. Besides, the performance of SDGKS was also evaluated with both inviscid and viscous flows. The numerical solutions match well with the analytic reference solutions. The future work will focus on extending the current method to triangular and mixed elements.

Acknowledgements

The authors would like to thank Dr. F.X. Zhao for helpful discussion on the SDGKS method.

The current research is supported by the National Natural Science Foundation of China (Grant 12172316) and by the Hong Kong Research Grant Council (Grants 16208021 and 16301222).

References

[1] A. Balan, G. May and J. Schöberl, *A stable high-order spectral difference method for hyperbolic conservation laws on triangular elements*, J. Comput. Phys. **231**, 2359–2375 (2012).

[2] F. Bassi and S. Rebay, *A high-order accurate discontinuous finite element method for the numerical solution of the compressible Navier-Stokes equations*, J. Comput. Phys. **131**, 267–279 (1997).

[3] P.L. Bhatnagar, E.P. Gross and M. Krook, *A model for collision processes in gases. I. Small amplitude processes in charged and neutral one-component systems*, Phys. Rev. **94**, 511 (1954).

[4] G. Cao, H. Liu and K. Xu, *Physical modeling and numerical studies of three-dimensional non-equilibrium multi-temperature flows*, Phys. Fluids **30**, 126104 (2018).

[5] P. Castonguay, P.E Vincent and A. Jameson, *A new class of high-order energy stable flux reconstruction schemes for triangular elements*, J. Sci. Comput. **51**, 224–256 (2012).

[6] M. Coutanceau and R. Bouard, *Experimental determination of the main features of the viscous flow in the wake of a circular cylinder in uniform translation. Part 1. Steady flow*, J. Fluid Mech. **79**, 231–256 (1977).

[7] X. Ji, W. Shyy and K. Xu, *A p-multigrid compact gas-kinetic scheme for steady-state acceleration*, Comput. & Fluids **241**, 105489 (2022).

[8] X. Ji, F. Zhao, W. Shyy and K. Xu, *A family of high-order gas-kinetic schemes and its comparison with Riemann solver based high-order methods*, J. Comput. Phys. **356**, 150–173 (2018).
[9] M. Li, Z. Qiu, C. Liang, M. Sprague, M. Xu and C.A. Garris, *A new high-order spectral difference method for simulating viscous flows on unstructured grids with mixed-element meshes*, Comput. & Fluids **184**, 187–198 (2019).
[10] Q. Li, K. Xu and S. Fu, *A high-order gas-kinetic Navier-Stokes flow solver*, J. Comput. Phys. **229**, 6715–6731 (2010).
[11] C. Liang, S. Premasuthan, A. Jameson and Z.J. Wang, *Large eddy simulation of compressible turbulent channel flow with spectral difference method*, in: *47th AIAA Aerospace Sciences Meeting including The New Horizons Forum and Aerospace Exposition*, 402 (2009).
[12] X. Liang, X. Min, Z. Bin and Q. Zihua, *A new spectral difference method using hierarchical polynomial bases for hyperbolic conservation laws*, J. Comput. Phys. **284**, 434–461 (2015).
[13] C. Liu and K. Xu, *A unified gas kinetic scheme for continuum and rarefied flows V: Multiscale and multi-component plasma transport*, Commun. Comput. Phys. **22**, 1175–1223 (2017).
[14] C. Liu, K. Xu, Q. Sun and Q. Cai, *A unified gas-kinetic scheme for continuum and rarefied flows IV: Full Boltzmann and model equations*, J. Comput. Phys. **314**, 305–340 (2016).
[15] Y. Liu, M. Vinokur and Z.J. Wang, *Spectral difference method for unstructured grids I: Basic formulation*, J. Comput. Phys. **216**, 780–801 (2006).
[16] H. Luo, L. Luo and K. Xu, *A BGK-based discontinuous Galerkin method for the Navier-Stokes equations on arbitrary grids*, in: *Computational Fluid Dynamics Review 2010*, pp. 103–122, World Scientific (2010).
[17] G. May and J. Schöberl, *Analysis of a Spectral Difference Scheme with Flux Interpolation on Raviart-Thomas Elements*, Aachen Institute for Advanced Study in Computational Engineering Science **410** (2010).
[18] M.L. Minion and D.L. Brown, *Performance of under-resolved two-dimensional incompressible flow simulations, II*, J. Comput. Phys. **138**, 734–765 (1997).
[19] L. Pan, J. Cheng, S. Wang and K. Xu, *A two-stage fourth-order gas-kinetic scheme for compressible multicomponent flows*, Commun. Comput. Phys. **22**, 1123–1149 (2017).
[20] L. Pan and K. Xu, *Two-stage fourth-order gas-kinetic scheme for three-dimensional Euler and Navier-Stokes solutions*, Int. J. Comput. Fluid Dyn. **32**, 395–411 (2018).
[21] L. Pan, K. Xu, Q. Li and J. Li, *An efficient and accurate two-stage fourth-order gas-kinetic scheme for the Euler and Navier-Stokes equations*, J. Comput. Phys. **326**, 197–221 (2016).
[22] J. Park, K. Kwon and H. Choi, *Numerical solutions of flow past a circular cylinder at Reynolds numbers up to 160*, KSME Int. J. **12**, 1200–1205 (1998).
[23] M. Parsani, G. Ghorbaniasl and C. Lacor, *Validation and application of an high-order spectral difference method for flow induced noise simulation*, J. Comput. Acoust. **19**, 241–268 (2011).
[24] M. Parsani, G. Ghorbaniasl, C. Lacor and E. Turkel, *An implicit high-order spectral difference approach for large eddy simulation*, J. Comput. Phys. **229**, 5373–5393 (2010).
[25] X. Ren, K. Xu and W. Shyy, *A multi-dimensional high-order DG-ALE method based on gas-kinetic theory with application to oscillating bodies*, J. Comput. Phys. **316**, 700–720 (2016).
[26] X. Ren, K. Xu, W. Shyy and C. Gu, *A multi-dimensional high-order discontinuous Galerkin method based on gas kinetic theory for viscous flow computations*, J. Comput. Phys. **292**, 176–193 (2015).
[27] V.V. Rusanov, *The calculation of the interaction of non-stationary shock waves and obstacles*, USSR Comput. Math. Math. Phys. **1**, 304–320 (1962).
[28] B. Sharman, F.S. Lien, L. Davidson and C. Norberg, *Numerical predictions of low Reynolds number flows over two tandem circular cylinders*, Int. J. Numer. Meth. Fluids **47**, 423–447 (2005).

[29] Y. Sun, Z.J. Wang and Y. Liu, *High-order multidomain spectral difference method for the Navier-Stokes equations*, In 44th AIAA Aerospace Sciences Meeting and Exhibition, 301 (2006).
[30] D.J. Tritton, *Experiments on the flow past a circular cylinder at low Reynolds numbers*, J. Fluid Mech. **6**, 547–567 (1959).
[31] K.Van den Abeele, C. Lacor and Z.J. Wang, *On the stability and accuracy of the spectral difference method*, J. Sci. Comput. **37**, 162–188 (2008).
[32] Z.J. Wang, Y. Liu, G. May and A. Jameson, *Spectral difference method for unstructured grids II: Extension to the Euler equations*, J. Sci. Comput. **32**, 45–71 (2007).
[33] K. Xu, *A gas-kinetic BGK scheme for the Navier-Stokes equations and its connection with artificial dissipation and Godunov method*, J. Comput. Phys. **171**, 289–335 (2001).
[34] K. Xu, M. Mao and L. Tang, *A multidimensional gas-kinetic BGK scheme for hypersonic viscous flow*, J. Comput. Phys. **203**, 405–421 (2005).
[35] L.J. Xuan and K. Xu, *An efficient high-order finite difference gas-kinetic scheme for the Euler and Navier-Stokes equations*, Comput. & Fluids **166**, 243–252 (2018).
[36] C. Zhang, Q. Li, S. Fu and Z. Wang, *A third-order gas-kinetic CPR method for the Euler and Navier-Stokes equations on triangular meshes*, J. Comput. Phys. **363**, 329–353 (2018).
[37] F. Zhang, J. Cheng and T. Liu, *A direct discontinuous Galerkin method for the incompressible Navier-Stokes equations on arbitrary grids*, J. Comput. Phys. **380**, 269–294 (2019).
[38] F. Zhao, X. Ji, W. Shyy and K. Xu, *Compact higher-order gas-kinetic schemes with spectral-like resolution for compressible flow simulations*, Adv. Aerodyn. **1**, 13 (2019).